Feasibility of Bone Fracture Detection Using Microwave Imaging

KESIA C. SANTOS [1,2] **(Student Member, IEEE), CARLOS A. FERNANDES** [1] **(Senior Member, IEEE), AND JORGE R. COSTA** [1,3] **(Senior Member, IEEE)**

[1]Instituto de Telecomunicações, Instituto Superior Técnico, 1049-001 Lisbon, Portugal

[2]Unidade de Indústria, Instituto Federal da Paraíba, João Pessoa 58015-435, Brazil

[3]DCTI, Instituto Universitário de Lisboa (ISCTE-IUL), 1649-026 Lisbon, Portugal

CORRESPONDING AUTHOR: K. C. SANTOS (e-mail: kesia.farias@ifpb.edu.br).

ABSTRACT This paper studies the feasibility of Microwave Imaging (MWI) for detection of fractures in superficial bones like the tibia, using a simple and practical setup. First-responders could use it for fast preliminary diagnosis in emergency locations, where X-Rays are not available. It may prove valuable also for cases where X-ray are not recommended, e.g., length pregnant women or children. The method is inspired on the synthetic aperture radar technique. A single Vivaldi antenna is used to linearly scan the bone in the 8.3-11.1 GHz frequency range and collect the scattered fields. The system is operated in air, without the need for impractical impedance-matching immersion liquids. The image is reconstructed using a Kirchhoff migration algorithm. A Singular Value Decomposition (SVD) strategy is used to remove skin and background artifacts. To test this technique, a set of full-wave simulations and experiments were conducted on a multilayer phantom and on an ex-vivo animal bone. Results show that the system can detect and locate bone transverse fractures as small as 1 mm width and 13 mm deep, even when the bone is wrapped by 2 mm thick skin.

INDEX TERMS Biomedical imaging, bones, dielectric materials, image reconstruction, microwave imaging.

I. INTRODUCTION

THE DETECTION and monitoring of fractures in bones can be performed by using several medical imaging techniques, such as X-rays scan, Computed Tomographic (CT) scan and Magnetic Resonance Imaging (MRI) scan. In general, the X-ray is the first screening test performed when the patient arrives at the hospital. Due to the high cost, CT and MRI are indicated only in cases where X-rays do not provide the necessary detail [1]. MRI provides better contrast between cortical bone, bone marrow, muscle, and soft tissues in the body, yet it is the most expensive and slower technique [2]. X-rays and CT scan are ionizing, therefore potentially pose some degree of health risk.

The risk of falling and suffering fractures is very common in children and elderly people. Tibia fractures are the third most frequent long bone fractures in children with 15% occurrence [3], [4]. Considering that fractures in superficial bones are frequent, it would be beneficial to have an alternative non-ionizing and non-invasive screening method, for first response screening in ambulances, retirement houses, pregnant women, newborn, and infants, or in low-income settings. A microwave system shall achieve those objectives, being useful also for subsequent fracture healing monitoring. The system is potentially inexpensive, compact, and portable.

The overall idea is to use a scanning microwave monostatic radar system for detecting the bone permittivity discontinuity at the fracture. The scattered fields from healthy and injured

tissues can be retrieved and processed to identify the fracture location.

Microwave imaging (MWI) has been extensively studied for detection of early breast cancer [5], for tears in the meniscus [6], and for brain hemorrhage [7]. In [8], the reconstruction of bone profiles is investigated using a manufactured uniform phantom geometry prepared with animal tissues (tibia, fibula, muscle, and fat). The whole system is immersed in a coupling medium composed of a complex mixture. Immersion of a body part is not appropriate for a practical application, adding discomfort to the patient and sanitation issues. Moreover, the objective in [8] is not related to bone fracture detection.

In [9], an experimental setup without matching medium is used inside an anechoic chamber, to study extensive longitudinal lesions (radius of 3 mm and extension of 130 mm) implanted in a uniform artificial phantom geometry composed of three plastic tubes filled with liquids mimicking the cortical bone, bone marrow and longitudinal lesion. Muscle and skin are not considered in the phantom. In [10], the authors used an adapted free space setup, based on a previous clinical prototype Mammowave, to detect longitudinal bone fractures and lesions in a simplistic uniform phantom geometry without considering the skin. The solution requires a fixed and bulky setup, which limits the portability and increases the cost for practical applications.

In [11], the authors proposed a portable system to detect transversal bone fractures using a planar electromagnetic bandgap sensor with 11.4 mm X 80 mm dimension in contact with the patient's skin. A realistic phantom composed of human tibia, muscle, fat, and porcine skin is used, with fractures of 2 mm and 1 mm. The method relies on the analysis of the deviation of the resonant frequency of a sensor in the presence of bone fracture. The requirement of firm contact between the non-conformal sensor and patient's skin during scanning may be difficult to achieve in practice. According to the authors, a 100 μm gap between the sensor and the skin causes a 5% error in frequency deviation, therefore the measurement reliability may be affected by non-uniformity of skin contact in successive measurement points.

Our study addresses the feasibility of contactless MWI detection of thin transverse bone fractures, considering simultaneously the practicality of the setup for a real application and trying to overcome the shortcomings of the previous studies. This includes eliminating the need for immersion liquids that are otherwise widely used to reduce the skin artifact but are not practical for a field-operated system. Contactless operation brings new challenges for fracture detection since the skin response now largely overshadows the fracture response. We note that unlike irrigated tissues such as tumors, the contrast from bone tissue cracks may be very weak. This is one of the main issues tackled in this paper, using a singular value decomposition (SVD)-based strategy to filter out precisely the unwanted reflections from the skin and thee bone itself.
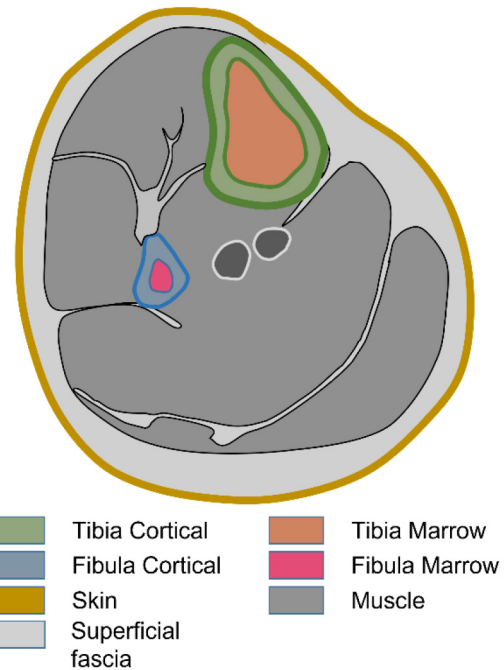

FIGURE 1. Cross-sectional anatomy of the leg. Adapted from [14].

The second new contribution of this paper is to demonstrate the concept feasibility using a very simple setup for future practical implementation, based on a single linear scan antenna operating in monostatic radar mode, in air.

Finally, the feasibility tests involve not only full-wave simulations with equivalent numerical models of the tibia, fibula, and surrounding tissues, with proper dielectric properties, but also experimental tests with *ex-vivo* animal bone and skin. The dielectric properties of the used animal tissues were measured in-house.

Based on usual image quality metrics, the proposed setup is shown to detect transverse fractures as thin as 1 mm, and 13-mm deep. The authors reported a preliminary evaluation of this approach, based on simulation in [12] and experimentally in [13], which served as the base for the new developments described in this paper.

Table 4 shows the comparison between our proposed MWI system to detect bone fractures with existing ones (see the Appendix). To the best of author's knowledge, no other publication has tackled concomitantly the issue of small transversal bone fracture detection, the constrains of a contactless air-operated system appropriate for a practical set-up, and the demonstration of its performance using real biological bones.

II. BONE MORPHOLOGY AND DIELECTRIC CHARACTERISTICS

The leg is composed of a heterogeneous combination of different tissues: bones, muscles, tendons, veins, arteries and nervous, as shown in the Fig. 1. It is adapted from the 20th U.S. edition of Gray's Anatomy of the Human Body [14]. The leg bones are the tibia and fibula. We can observe
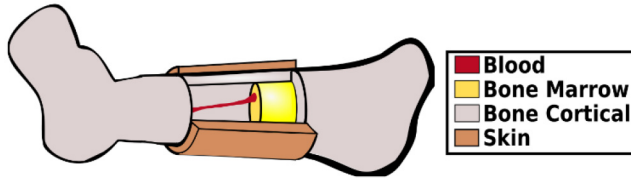
FIGURE 2. Schematic diagram of a portion of a tibia bone.

that the medial side of the tibia is subcutaneous, without muscle overlay. This favors microwave penetration at higher microwave frequencies, therefore higher potential resolution to resolve small fractures.

Before testing the proposed microwave imaging technique on real biological models, a simplified representation of the bone was used in a first step, both for the numerical model and for the experimental phantom. A uniform cylindrical geometry was defined first, representing the tibia with dielectric properties of cortical bone. This step was useful to gather insight about the detection of fractures and to identify the critical factors that impair the detection, without geometry-related confounder effects.

The phantom model was subsequently improved in the subsequent sections, to approach the real bone shape and structure, including the consideration of a real biological bone in the experimental evaluation. Fig. 2 shows the simplified material layering adopted in the numerical models of the *ex-vivo* samples. The cortical bone and marrow bone are considered as a single homogeneous medium for image reconstruction purpose, with dielectric characteristics (ε, σ) equivalent to the cortical bone since this is the most external bone layer. The muscular tissue is not considered in the model since we are modelling the part of the tibia where it becomes most superficial. Our phantom includes a skin layer covering the bone tissue [15], [16]. When a fracture occurs, it ruptures several internal small blood vessels filling the fracture with blood. This is also properly accounted both in the numerical model and in the phantoms. The complex permittivity of these materials is well known [17], [18], [19].

Tissues dielectric properties change from patient to patient. Mainly, there is an age-dependency of its dielectric properties, and this is correlated to the amount of water, which varies with age [20], [21], [22]. As will be demonstrated ahead, the method is quite robust to these variations.

A. MIMICKING LIQUID MIXTURES

A key requirement to produce a usable phantom is to be able to reproduce as close as possible the dielectric properties of the actual biological tissues. There are known recipes for liquid mixtures that can mimic various biological tissues. After preparing them, and often storing them for long periods, it is important to verify experimentally how well the mixtures reproduce the actual electromagnetic response of biological tissues described in the literature [19].

TABLE 1. Recipes of liquids mixtures.

Tissue	TX – 100	Distilled Water	NaCl
Cortical bone	75%	25 %	0.8 g/L
Blood	14%	86%	9 g/L

TABLE 2. Parameters corresponding to in-house measured phantom mixtures.

	ε_∞	$\Delta\varepsilon_1$	$\Delta\varepsilon_2$	τ_1 (ps)	τ_2 (ns)	α_1	α_2	σ (S/m)
Bone Cortical	2.5	15.5	45	52	100	0.1	0.1	0.01
Blood	4	56	5200	8.4	138.6	0.2	0.2	0.7

One of those liquid mixtures consists of Triton X-100 (TX-100) and distilled water [17]. A recipe is presented in [23] that mimics cortical bone and blood, in the 1-6 GHz band. It was verified that the same recipe can be used to mimic the dielectrics properties of bone tissue in the 8.3-11.1 GHz band [19], as shown in Table 1.

Measurements of the complex permittivity were conducted after the fabrication of the liquid mixtures, using two different methods for cross-validation: the open–ended coaxial probe and a coaxial cavity [24], [25]. The first method is a golden standard that lends to the dielectric property values versus frequency using closed form expressions [26]. The coaxial cavity method, used in [27], uses an indirect approach that involves comparison of measurement results with those obtained by full-wave simulations for the same test mixture. The simulation requires the assumption of a dispersion model for the sample under analysis. For that purpose, the multi-term Cole-Cole model was adopted as in [22]:

$$\varepsilon^* = \varepsilon_\infty + \sum_n \frac{\Delta\,\varepsilon_n}{1+(j\omega\tau_n)^{1-\alpha_n}} + \frac{\sigma}{j\omega\varepsilon_0} \qquad (1)$$

where ω is the angular frequency, σ is the conductivity, n sets the number of terms, τ_n is the relaxation time, α_n is a measure of the broadening of the dispersion of the nth terms, $\Delta\,\varepsilon_n = \varepsilon_{s,n} - \varepsilon_\infty$, where $\varepsilon_{s,n}$ and ε_∞ are the static and infinite frequency dielectric constants, respectively. In the present study, the dielectric properties of the mixtures were modeled using n = 2 order. The corresponding best-fit parameters were determined through the method described in [28], and are shown in Table 2.

Fig. 3 shows the dielectric properties results of the fabricated phantom, calculated using both methods. The results are compared with the reference properties for biological tissues defined in [19]. The agreement is good.

III. IMAGING ALGORITHM

Consider the geometry shown in Fig. 4 that represents a bone with its length aligned with the *x*-axis, and with a transverse fracture. The antenna performs a linear scan parallel to the *x*-axis, in the *xz*-plane. P_{Bone} designates the bone boundary at coordinates $(x_{Bone}, y_{Bone}, z_{Bone})$, while (x, y, z) defines the test point P inside the bone.
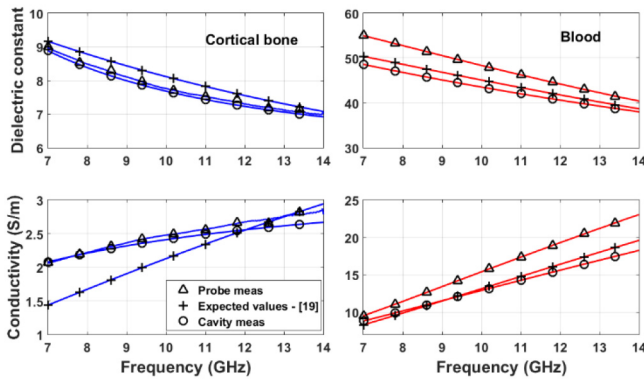
FIGURE 3. Dielectric properties of the fabricated mixtures mimicking cortical bone (blue lines) and blood (red lines) human tissues. Crosses represent the expected values corresponding to biological tissues [19].
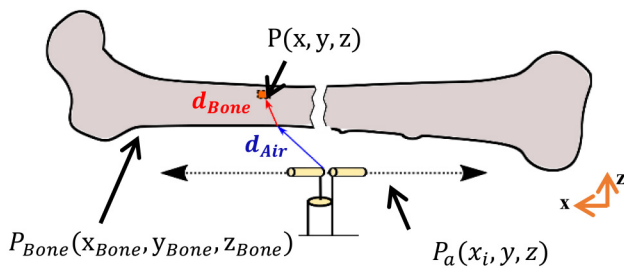

FIGURE 4. Representation of the microwave imaging setup with an antenna operated in radar mode, linear scan on the x-axis and depth on the z-axis.

The antenna produces linear polarization along the *x*-axis, and operates in the very near region of the bone.

The antenna acquires $s_{11}(x_i, f_l)$ at $i = 1 \cdots N_a$ uniformly distributed antenna positions $P_a(x_i, \ y, \ z)$, and at each of these positions, scans $l = 1 \cdots N_f$ frequencies in the [8.3 − 11.1] GHz range. Uniform spacing is not required by the method if the coordinates are known. The image is reconstructed in the same plane that contains the antenna travel path and the *z*-axis; therefore, the imaging algorithm is treated as a 2D problem.

The measured $s_{11}(x_i, f_l)$ signal contains two main contributions: the antenna internal reflections and the external scattered signals picked-up by the antenna. Therefore, further pre-processing of the signal is applied to remove the unwanted contributions. In a first step, a simple filtering is applied to $s_{11}(x_i, f_l)$, by subtracting the average of all N_a antenna positions:

$$s_{11}^{cal}(x_i, f_l) = s_{11}(x_i, f_l) - \overline{s_{11}(x_i, f_l)} \qquad (2)$$

where $s_{11}^{cal}(x_i, f_l)$ is the signal with reduced artifacts.

In situations where the bone/phantom is covered with skin, one more pre-processing step is required. The $s_{11}^{cal}(x_i, f_l)$ function contains the bone fracture signature, but it is severely masked by dominant reflections from the very close air-skin interface and, to a lesser extent, by the contribution of other scatterers present in the measurement scenario. These unwanted signals that persist after (2) create artifacts

in the reconstructed image. Different strategies exist for the skin artifact removal [7], [28], [29], [30], [31].

We used the Singular Value Decomposition (SVD) to separate the signal scattered from the target into different contributions, the ones from the skin, fracture, and background. SVD is used to reduce clutter in landmine [32], and in through-the-wall imaging [33]. It is also used to separate signals from the tumor and background in [30] and [34] for breast cancer detection.

The $s_{11}^{cal}(x_i, f_l)$ matrix is decomposed using the SVD, such as presented in (3), in which U is the unitary matrix of left singular values, V^H is the Hermitian of the unitary matrix of right singular values. The variable Σ represents a square diagonal matrix composed of the single values σ_k of s_{11}^{cal} ordered in descending sequence. The maximum value of k is the rank of the matrix s_{11}^{cal}.

$$s_{11}^{cal}(x_i, f_l) = U\Sigma V^H = \sum_{k=1}^{N} \sigma_k u_k v_k^H \qquad (3)$$

The decreasing sequence of the single values means that the first elements are related with the higher levels of signal reflection. Our setup is based on the measurement of the reflected signal. Thus, it is necessary to separate the desired reflections (fracture) from the undesired (skin, bone non-uniform profile).

Because of the non-uniform geometry of the bone, reflections from its boundary and skin may change significantly over the scanned area. The fracture scattered signal may be overshadowed by these non-uniformities if SVD is applied on the full scan vector at once, in [34] this method is used to reconstruct a uniform shape. Considering non-uniform shapes, an interesting strategy is to divide the scanned area into smaller subregions, in which the backscattered signal can be considered locally similar [35].

$$\begin{aligned} & s_{11}^{cal}(x_i, f_l) \\ &= \left[s_{11}^{cal}(x_{R1}, f_l) \ \cdots \ s_{11}^{cal}(x_{Rq}, f_l) \cdots \ s_{11}^{cal}(x_{RQ}, f_l) \right] \end{aligned} \quad (4)$$

Equation (3) is then applied to each subregion $s_{11}^{cal}(x_R, f_l)$. All the subregion vectors are non-overlapping and contain the same number of antenna positions. In (4) the number of subregions is Q, each one with Na/Q elements. To exemplify, the first subregion is composed by the subset $s_{11}^{cal}(x_{R1}, f_l) = \{s_{11}^{cal}(x_1, f_l), \ s_{11}^{cal}(x_2, f_l), \ldots s_{11}^{cal}(x_{Na/Q}, f_l)\}$. The results presented in this paper considers Q=3, this value was chosen based on empirical tests.

Based on experimental analysis, the most relevant undesired reflections are represented by the first and/or second singular values, depending on the scenario. In all subregions, the same number of singular values are removed. Therefore, the SVD filtered response is expressed by (5), where g = 2 for scenarios with skin, and g = 1 for scenarios without skin:

$$s_{11}^{s}(x_R, \ f_l) = \sum_{k=g}^{N} \sigma_k u_k v_k^H \qquad (5)$$

After this step, the s_{11}^s matrix of the complete scan is rearranged by concatenating the subregion results $s_{11}^s(x_R, f_l)$.

Consider the $\mathbf{R}'$ matrix, which represents the back-scattered response from each pixel under analysis in the xz-plane, for each of the N_f frequencies:

$$\mathbf{R}' = \begin{bmatrix} \mathbf{r}'_{11} & \cdots & \mathbf{r}'_{m1} \\ \vdots & \ddots & \vdots \\ \mathbf{r}'_{1n} & \cdots & \mathbf{r}'_{mn} \end{bmatrix} \tag{6}$$

where $m = 1 \cdots N_{px}, n = 1 \cdots N_{pz}$ represent pixel indexes along x and z coordinates. The matrix elements are calculated using the range migration algorithm [36]

$$\mathbf{r}'_{mn}(f_l) = \frac{1}{N_a} \sum_{i=1}^{N_a} s_{11}^s(x_i, f_l)\ e^{j\ 2\ \mathbf{k_0}\ D_{i(m,n)}}$$
$$= \left\{ \mathbf{r}'_{mn}(f_1),\ \mathbf{r}'_{mn}(f_2), \ldots, \mathbf{r}'_{mn}(f_{N_f}) \right\} \tag{6a}$$

where $\mathbf{k}_0$ represents the set of free-space wave-numbers calculated for each of the N_f frequencies. It is free from spurious scattering and denotes the complete set of values for all N_f frequencies. $D_{i(m,n)}$ represents the total electrical distance from each antenna position $P_a(x_i)$ to each (m, n) test pixel in the image reconstruction xz-plane:

$$D_{i(m,n)} = d_0 + \sqrt{\varepsilon_{r1}}d_1 + \sqrt{\varepsilon_{r2}}d_2 + \cdots \sqrt{\varepsilon_{rq}}d_q \tag{6b}$$

where d_0 is the path length between the P_a antenna position and the entry point P_{Bone} at the first layer boundary, and d_1, $d_2 \cdots d_q$ are the lengths travelled in each tissue according to Snell's laws.

The image can be reconstructed from:

$$\mathbf{I}' = \begin{bmatrix} I'_{11} & \cdots & I'_{m1} \\ \vdots & \ddots & \vdots \\ I'_{1n} & \cdots & I'_{mn} \end{bmatrix} \tag{7}$$

where

$$I'_{mn} = \left| \sum_{l=1}^{N_f} \mathbf{r}'_{mn}(f_l) \right|^2 / (N_f)^2 \tag{7a}$$

At each test pixel where a target (fracture) exists, the sums in (6a) and (7a) add up coherently increasing its value with N_a and N_f. Otherwise, the signals add-up incoherently, and the sum tends to zero.

Note that $\mathbf{r}'_{mn}(f_l)$, with dimension $[N_f]$, already adds up the N_a antenna contributions. In I'_{mn} the frequencies are also summed, considering the contributions of all antenna positions and frequencies to the (m, n) pixel.

However, the unknown actual thickness of fat and muscle layers, and of the curvature of the bone in real applications, may cause additional image artifacts. These occur near the skin for shallow z-values, while the response from the fracture extends to deep z-values. Therefore, by averaging the response over z, it is possible to decrease the influence of these artifacts, without affecting the fracture response. The high resolution along cross range (the x-coordinate) is

ensured by the used synthetic aperture type of algorithm, and by the near-field effect of the antenna. For this purpose, we mind that the $\mathbf{R}'$ matrix columns are slices in z direction composed of the summation of all antenna contributions. A weight factor is introduced to increase the relevance, in amplitude, of the deeper signal.

$$\boldsymbol{\phi_m}(f_l) = \left\{ \left\langle \mathbf{r}'_{mn}(f_1) \right\rangle_z,\ \left\langle \mathbf{r}'_{mn}(f_2) \right\rangle_z, \ldots \right\}$$
$$= \left\{ \mathbf{r}'_m(f_1),\ \mathbf{r}'_m(f_2), \ldots,\ \mathbf{r}'_m(f_{N_f}) \right\} \tag{8}$$

where $\langle \cdot \rangle_z$ represents the mean over the pixels along z. This calculation eliminates the dimension n of the matrix. Function $\boldsymbol{\phi_m}(f_l)$ represents the desired mean along z. We normalize it dividing $\boldsymbol{\phi_m}(f_l)$ by its mean value in frequency:

$$\boldsymbol{\varphi_m}(f_l) = \frac{1}{\left\langle \mathbf{r}'_m(f_l) \right\rangle_f} \left\{ \mathbf{r}'_m(f_1),\ \mathbf{r}'_m(f_2) \cdots \right\} \tag{9}$$

To understand better how the weight function is used, it is useful to use (6a) and expand the sum in (7a), which gives the magnitude of the image pixel:

$$I'_{mn} = \left| s_{11}^s(x_1, f_1)e^{j\ 4\ \frac{\pi\ f_1}{c}D_{i(m,n)}} \right.$$
$$+ s_{11}^s(x_2, f_1)e^{j\ 4\ \frac{\pi\ f_1}{c}D_{i(m,n)}} + \cdots$$
$$+ s_{11}^s\left(x_{N_a}, f_{N_f}\right)e^{j\ 4\ \frac{\pi\ f_{N_f}}{c}\ D_{i(m,n)}} \left. \right|^2 / (N_a N_f)^2 \tag{10}$$

With the proposed method, the image is reconstructed instead by using an alternative modified version of (10) for each pixel, obtained through the following dot product:

$$I_{mn} = \left| \mathbf{r}'_{mn}(f_l) \cdot \boldsymbol{\varphi_m}(f_l) \right|^2 / N_f^2 \tag{11}$$

The dot product in (11) reproduces the sum in (10) but becomes a weighted sum. We call this proposed method the "weighting procedure". The total image is obtained from the modified matrix:

$$\mathbf{I} = \begin{bmatrix} I_{11} & \cdots & I_{m1} \\ \vdots & \ddots & \vdots \\ I_{1n} & \cdots & I_{mn} \end{bmatrix} \tag{12}$$

We use two performance indicators to quantify the quality of the image reconstruction algorithm: signal-to-clutter ratio (SCR) and signal-to-mean ratio (SMR) [28], [29]. SCR is defined as the ratio between the maximum intensity corresponding to response in the fracture region, S, and the maximum intensity of the background clutter response, C, within the scanned region.

$$SCR\ [dB] = 10 log_{10}(max(S)/max(C)) \tag{13}$$

SMR is defined as the ratio between the maximum intensity corresponding to response in the fracture region, S, and the mean intensity of the background medium clutter response, C, in the scanned region.
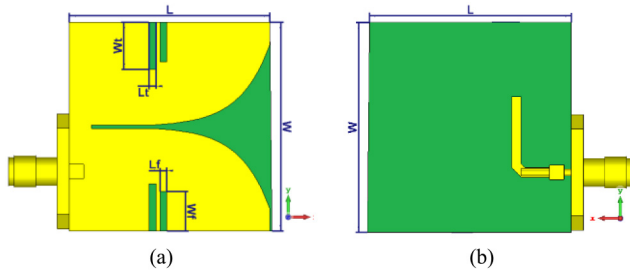
$$SMR\ [dB] = 10 log_{10}(max(S)/mean(C)) \tag{14}$$

FIGURE 5. Vivaldi Antenna designed for this application, (a) front; (b) back.

FIGURE 6. (a) Vivaldi antenna prototype and (b) Simulated and measured reflection coefficient of the antenna in free-space.

It is important to emphasize that in a realistic clinical scenario, it is not possible to know in advance the exact geometry of the bone, the skin thickness, or the position of the fracture. For that reason, the presented formulation does not require, nor use that information. Knowledge of the bone fracture location is used only for metric calculations. The reconstruction procedure being otherwise obtained without using this information.Kesia C. Santos: Feasibility of Bone Fracture Detection using Microwave Imaging

IV. THE ANTENNA

The detection of small targets requires high-resolution images, which are obtained with the smallest possible wavelength and widest possible signal bandwidth. However, there is a tradeoff between achievable resolution and penetration depth in biological tissues. The latter decreases with increasing frequency. In this application, the tibia is a subcutaneous bone, which favors the use of higher frequencies than is usual in MWI.

Antennas in medical applications usually operate in the near field. It is desirable to use an antenna with small dimensions, wide bandwidth, and directional radiation pattern [37], [38]. These characteristics are not necessarily mutually compatible. This work uses a Vivaldi antenna as a compromise, operating in the frequency bandwidth 8.3-11.1 GHz. It is fabricated with ROGERS 5880 substrate, with $\varepsilon_r = 2.2$ and $\tan\delta = 0.0009$. It has an overall dimension $L \times W = 28.01 \times 29.1$ mm, Fig. 5. Slots were added to reduce the side lobe level, and to improve the radiation characteristics in the front-direction of the antenna. The feeding microstrip line was bent at 90 degrees to minimize unwanted reflections from the feeding cable [12].

The antenna design and all full-wave simulations in this study were performed in CST Microwave Studio®. The reflection coefficient (s_{11}) measured in free space is less than -10 dB over the frequency range of interest Fig. 6(b). The figure shows a frequency shift between measured and simulated curves, due to fabrication inaccuracies, however, we stress that this shift does not affect the detection results: in fact, our calibration process and SVD filtering removes mostly all antenna response within the frequency band of interest, which is preserved in the fabricated prototype. This will be confirmed ahead by the simple fact that the signal scattered by the fracture is clearly detected, despite its level
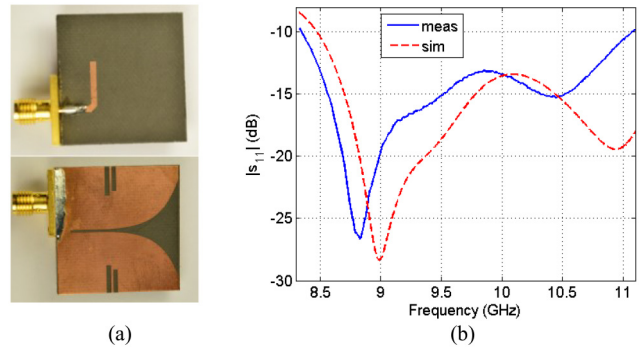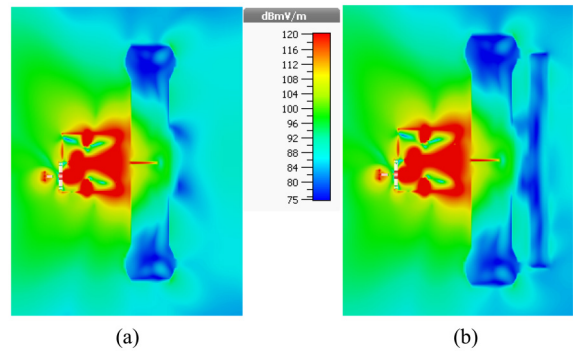

FIGURE 7. Simulation E-field distributions from Vivaldi antenna at 9 GHz on the xz-plane, the distance between the antenna and the bone is 6 mm, and the fracture is filled with blood. a) Bone (Tibia) and b) Bone (Tibia plus fibula).

being near 2 orders of magnitude lower than the antenna free space s_{11}.

It is very important to observe the near-field distribution of the antenna in the presence of the target (fracture filled with blood), to see how it penetrates the bone. This is shown in Fig. 7(a) for a tibia with a 1-mm thick fracture and Fig. 7(b) for the same fractured tibia in the presence of the fibula. In all cases, the fields penetrate the tibia well. It is also seen that the presence of the fibula does not significantly change the field distribution in the tibia region. In a real case, the fibula is deep seated inside the muscle; therefore, its actual influence will be even weaker.

By comparing the healthy bone with the fractured one, it is possible to quantify the amount of energy that penetrates the fracture. One possible way to quantify that, it is to calculate the Euclidian norm of the difference between the electric field in the fractured and healthy bones. The result is divided by the Euclidian norm of the electric field intensity of the healthy case. This normalized response ($||\mathbf{E}_{\text{health}} - \mathbf{E}_{\text{fracture}}||/||\mathbf{E}_{\text{health}}||$) presented in Fig. 8. In Fig. 8(a) the healthy reference corresponds to the tibia only, while in Fig. 8(b) the reference is the tibia plus fibula. The result is shown in dB scale since it represents a relative value. It is possible to observe that the field penetration in the fracture is intense, and that its value is the same independently of considering the fibula or not.
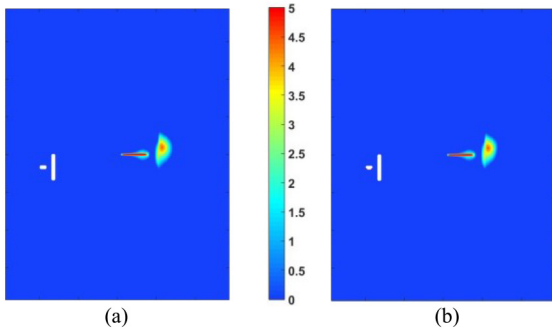
FIGURE 8. E-field penetration relative to the health bone scenario. a) Bone (Tibia) and b) Bone (Tibia plus fibula).
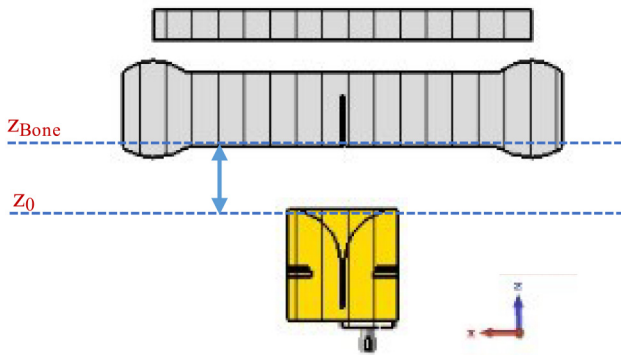

FIGURE 9. CST model representing an idealized tibia plus fibula. The distance between the antenna and bone is fixed at 6 mm.

V. FRACTURE DETECTION AND IMAGING PERFORMANCE

To validate the proposed strategy for fracture detection, the signals corresponding to the forward problem are obtained both from full wave simulations and from measurements. Different phantoms of the tibia with 1-mm thickness fracture are used, with increasing complexity, starting from mostly straight cylindrical phantoms to anatomical shape, with and without wrapping tissues, with or without the fibula, as well as biological bones with and without skin. The inverse problem, both for numerical and experimental data, is solved according to the formulation presented in Section III.

A. SIMULATION RESULTS

The general geometry of the reference scenario is presented in Fig. 9. The main bone is represented by a uniform 80 mm long cylindrical phantom with 19 mm diameter, terminated by enlarged sections. The adjacent bone is a uniform 100 mm cylinder with 7.6 mm diameter, and the distance between the cylinders' borders is 7.6 mm. We used mid-section tibial/fibular diameter ratio based on [39] and distance between their borders based on [14]. For both structures, we used cortical bone dielectric properties. A 1-mm thick, and 13-mm deep half-disc filled with blood phantom represents the fracture.

Following the nomenclature presented in Fig. 4, the antenna scans the tube for $N_a = 45$ equally spaced positions

TABLE 3. Average permittivity used for the biological tissues.

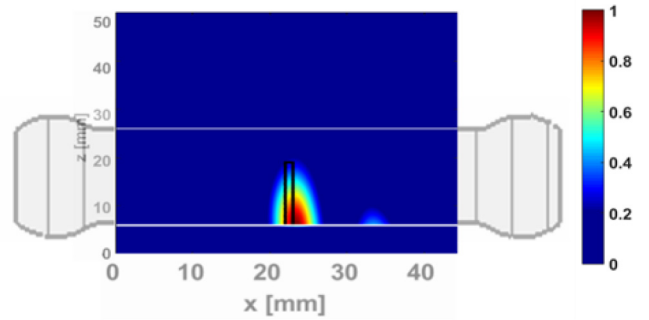| Tissue	ε_r	$\tan\delta$
Cortical bone	8	0.58 (mixture)
Blood	49	0.55 (mixture)

FIGURE 10. Reconstructed image of cylindrical phantom representing the fractured tibia ($z_{Bone} = 6$ mm), and fracture located at 22 $mm \leq x_{Bone} \leq 23$ mm filled with blood (1 mm), in a planar section. The black dotted contour identifies the fracture region. The antenna scans at 0 mm $\leq x_i \leq 44$ mm, $z = 0$.

between $P_a(x_1 = 0$ mm, 0, 0) and $P_a(x_{44} = 44$ mm, 0, 0) at $z = 0$. The fracture is located at 22 mm $\leq x_{Bone} \leq 23$ mm. The distance from the tip of the antenna to the bone is fixed at $z_{Bone} = 6$ mm. A range 6 mm $\leq z_{Bone} \leq 10$ offers a compromise between near-field resolution to escape the diffraction limit, and the perturbation caused by close interaction between the antenna and the tissue boundary. It is important to highlight, however, that for image reconstruction, the reference distance is the location of the antenna equivalent near-field phase center [30]. In each antenna position, the complex $s_{11}(x_i, f_l)$ is obtained by full-wave simulation over $N_f = 1001$ frequency points. The used the materials characteristics are shown in Table 3.

We show separately the reconstructed image of the tibia fracture without and with the influence of the fibula. The case without fibula is shown in Fig. 10. The energy map of the bone fracture in the xz-plane is calculated from (11). The scale is linear, normalized to the maximum intensity. The fracture is detected, and it is in the correct position marked with the dotted black lines. In this case SCR $= 3.4$ dB and SMR $= 18.5$ dB.

The result considering the influence of the fibula is shown in Fig. 11. Corresponding metrics are SCR $= 3.8$ dB and SMR $= 18.28$ dB, very close to the previous case. The reconstructed images are undistinguishable. This is in line with the almost unaffected near-field distribution discussed in the previous section, therefore, we will onwards disregard the fibula.Kesia C. Santos: Feasibility of Bone Fracture Detection using Microwave Imaging

B. EXPERIMENTAL RESULTS

Fig. 12 shows one of the measurement setups used in our lab. It consists of a Styrofoam platform that holds the phantom or biological bones. This platform attaches to an
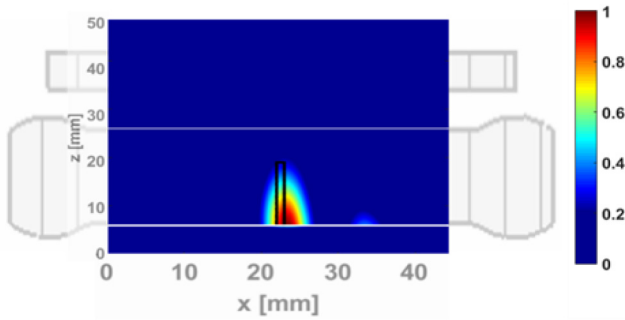
FIGURE 11. Reconstructed image of fractured tibia in the presence of the fibula (z_{Bone} = 6 mm), the fracture located at 22 $mm \leq x_{Bone} \leq$ 23 mm filled with blood (1 mm), in a planar section. The antenna scans at 0 mm $\leq x_i \leq$ 44 mm, z = 0. The black dotted contour identifies the fracture region.
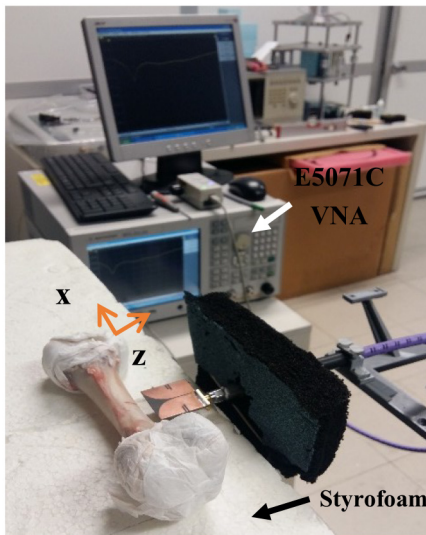

FIGURE 12. Details of the configuration of one of the microwave imaging systems.

FIGURE 13. Details of the 3D-PLA tube in mm.

(a)

(b)

FIGURE 14. (a) Fabricated bone phantom. (b) Bone phantom wrapped by an animal skin with thickness about of 2 mm and extension of 160 mm. The fracture is located about 46.5 mm $\leq$ x_Bone $\leq$ 47.5 mm.

automated linear translation stage, while the antenna is kept at a fixed position. This scanning configuration avoids the RF cable bending that might introduce undesirable phase and amplitude fluctuations. In a second setup, the phantom or bone lay stationary while the antenna scans its length. This configuration is closer to what is required in a practical application. In both setups, the system allows precise setting of the z-distance between the antennas and the bone phantom. An in-house automation code controls the linear stage movement and synchronous acquisition $s_{11}(x_i, f_l)$ using an Agilent E5071C Vector Network Analyzer (VNA).

1) TESTS WITH PHANTOMS

The model phantom is composed of a 3D-printed polylactic acid (PLA) cylinder, with 20-mm diameter, 154-mm length and permittivity $\varepsilon_r = 2.75$. The outer wall thickness is 1.25-mm. The hollow cylinder is divided in two parts by a 1-mm thick disk-shaped cross-section cavity, with 0.75 mm thick walls. The dimensions and model details are shown in Fig. 13. Although a more elaborate anthropomorphic phantom could be easily built, these simpler ones
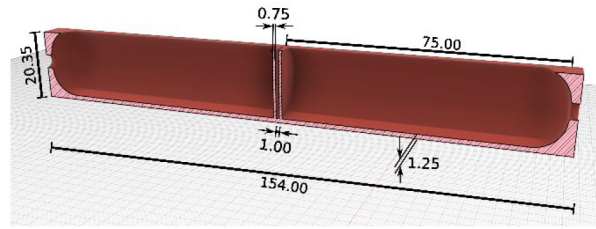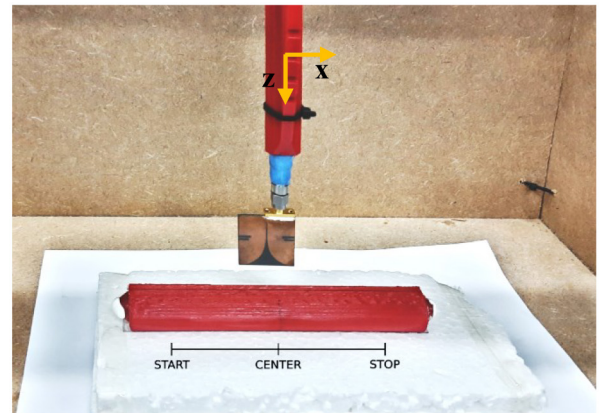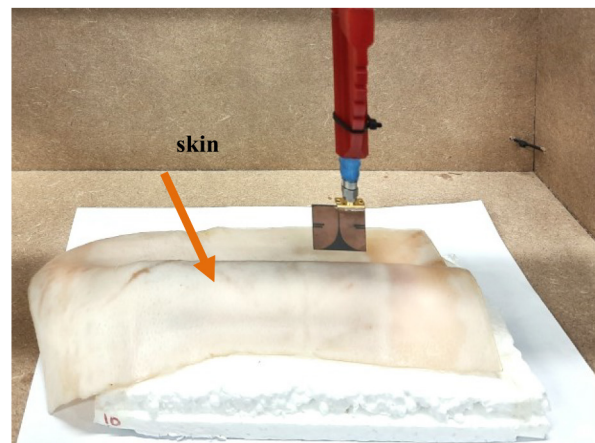
enable preliminary conclusions about fracture detection feasibility without confounding factors arising from specific geometries. Anyway, results obtained from *ex-vivo* biologic bones shown ahead are similar to the ones obtained with these phantoms, proving these models to be enough for that matter.

The complex-valued $s_{11}(x_i, f_l)$ was measured at equally spaced positions along the x-axis, $z = 0, y = 0$ over $N_f = 1001$ frequency points in the 8.3-11.1 GHz range. The scan comprised $N_a = 91$ points in the 0 mm $\leq x_i \leq$ 90 mm interval, with $z_i = 0, y_i = 0$.
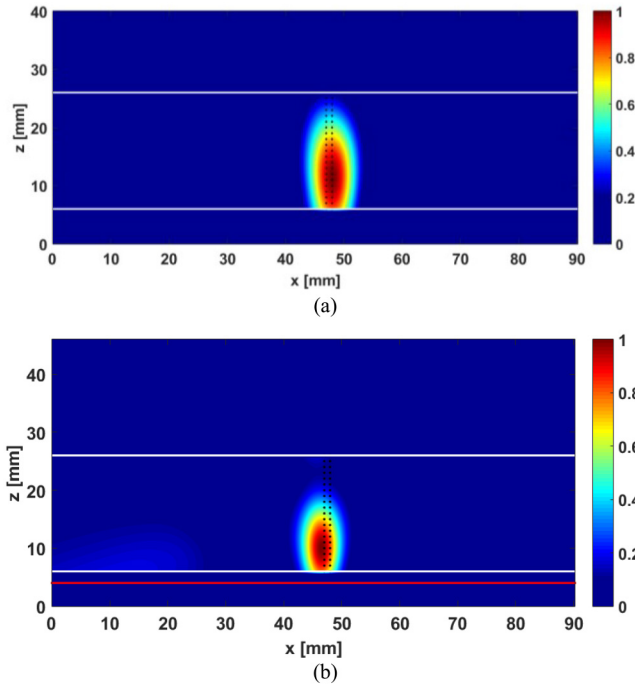
FIGURE 15. Reconstructed image on linear scale of cortical bone phantom, obtained from measurements, in a planar section. (a) simple phantom and (b) complete phantom wrapped with animal skin, the fracture is filled with blood (1 mm), in this case g = 2. The white contour identifies the bone limit. The black dotted contour identifies the fracture region. The red line identifies the skin limit. The antenna scan at 0 mm $\leq x_i \leq$ 90 mm and z = 0 The fracture is located about 46.5 mm $\leq x_{Bone} \leq$ 47.5 mm.

The phantom tube was filled with the fabricated mixtures that mimic cortical bone, while the cross-section disk was filled with a blood mimicking liquid (Fig. 14(a)). Fig. 14(b) shows the same fabricated bone phantom wrapped with *ex-vivo* animal skin (porcine skin) [14], with thickness of the order of 2 mm. The tip of the antenna was positioned $z_{Bone} = 6$ mm away from the phantom tube surface at its mid length. The reconstruction results for the phantom in the absence and in the presence of the animal skin layer are respectively shown in Fig. 15(a) and Fig. 15(b).

A positive fracture detection was found in both cases with and without skin. Although there is a good detection of the fracture, the image shows some artifacts that were not present in the bare phantom. They can only be attributed to skin imperfections or to air trapped between the skin and the phantom surface.

The metrics are SCR = 7.29 dB and SMR = 18.23 dB for the bare phantom, and SCR = 5.06 dB and SMR = 13.11 dB for the phantom covered with *ex-vivo* animal skin. These results confirm a quite good image quality and fracture detection.

2) TESTS WITH EX-VIVO BONES AND SKIN

A more realistic evaluation was performed using an animal tibia with 16-mm minimum diameter, and 80-mm length. A transverse cut was opened in the mid region of the bone, about 1-mm thick and 8-mm deep. In one of the tests,
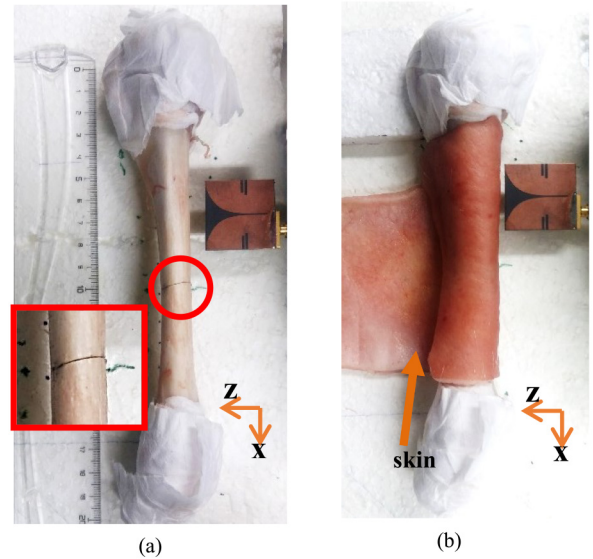

FIGURE 16. Representation of the measurement setup: (a) Animal bone. (b) Animal bone wrapped with an animal skin with thickness about of 2 mm and extension of 80 mm. The fracture is located about 24.5 mm $\leq x_{Bone} \leq$ 25.5 mm.
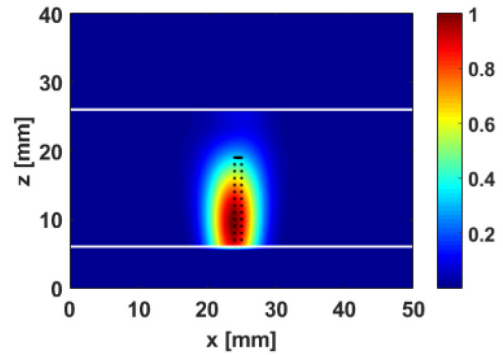

FIGURE 17. Reconstructed image on linear scale of *ex-vivo* animal bone obtained from measurements in a planar section. The fracture is about 1 mm. The white contour identifies the bone limit. The antenna scan at 0 mm $\leq x_i \leq$ 50 mm and, z = 0, in this case g =1.

the bone was wrapped with 2-mm thick porcine skin. Both tissues were kept refrigerated and hydrated until the measurement (Fig. 16). To increase the skin adhesion, we ensured that it was fresh skin at ambient temperature (around 25 °C), because at this temperature the viscosity and flexibility of the skin helps filling any air gap.

The tibia, with and without skin, was properly aligned with the scanning *x*-axis. The tip of the antenna was positioned at $z_{Bone} = 6$ mm away from the bone at its mid length. The scan comprised $N_a = 51$ points in the 0 mm $\leq x_i \leq$ 50 mm interval, with $z_i = 0, y_i = 0$. The result is shown in (Fig. 17). The fracture is well identified, as well as its right location despite the bone curved boundary, which changes the distance between the antenna and the bone. The metrics are SCR = 6.11 dB and SMR = 16.7 dB.

To highlight the achieved improvement with our proposed weighting strategy, we show the reconstructed image without and with the weighting procedure applied. The former

TABLE 4. Comparison of the state of the art on bone microwave imaging with our work.

| REF	MEDIUM	OBJECTIVE	PHANTOM	CONFIGURATION	COMMENT
[8]	Contact with the body patient	Reconstruction of bone profiles.	**Regular boundary tubes** using a manufactured phantom prepared with animal tissues (tibia, fibula, muscle, and fat);	**Two antennas** are used in the scan (s11 and s21 responses);	**Requires coupling medium** **Does not address fractures**
[10]	Free space Contactless with the body patient	Detecting **longitudinal bone fractures and lesions**	**Regular boundary tubes** representing the cortical bone, bone marrow, and a lesion; Longitudinal lesion (**radius of 3 mm and extension of 130 mm**).	**Two antennas** are used in the scan (s11 and s21 responses);	**Fractures are quite large** The system is bulky and expensive.
[11]	Free space **Contact with the body patient**	Detecting transversal bone fracture of about 1 mm	Realistic phantom composed of human tibia, muscle, fat, and porcine skin with **irregular boundary**	Uses a **planar sensor in contact with the patient's skin** (s11 and s21 responses).	Unrealistic precision is required for antenna contact with the body
OUR WORK	Free space **Contactless** with the body patient	Detecting transversal bone fracture of about 1 mm	Realistic phantom composed of animal tibia, and skin with **irregular boundary**	A **single antenna** is used in radar mode (s11 response)	
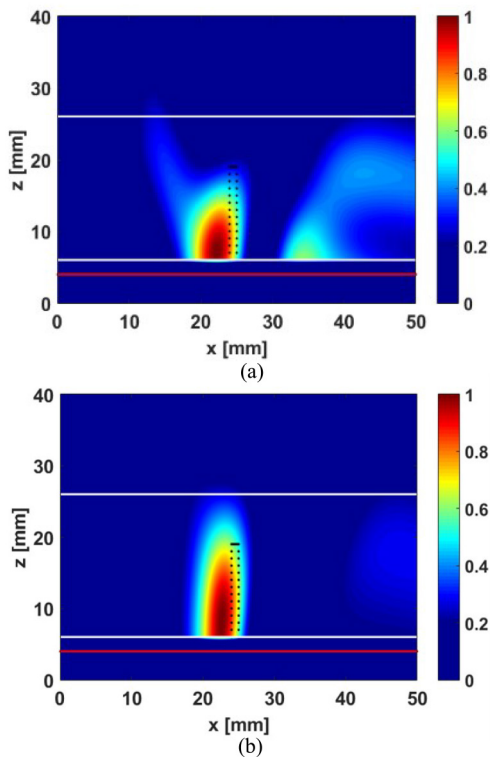
FIGURE 18. Reconstructed image on linear scale of *ex-vivo* animal bone wrapped with animal skin with thickness about of 2 mm, obtained from measurements, in a planar section (a) weighting procedure is not applied and (b) weighting procedure is applied. The fracture is about 1 mm thick. The white line identifies the bone limit. The red line identifies the skin limit. The antenna scan at $0\,\text{mm} \le x_i \le 50\,\text{mm}$ and, $z = 0$, with $g = 2$.

corresponds to Fig. 18(a), with metrics SCR = 2.1 dB and SMR = 10.24 dB. The latter corresponds to Fig. 18(b), with metrics SCR = 3.48 dB and SMR = 11.5 dB. The weighting procedure mitigates the effect of boundary irregularities.

The presence of artifacts in the image can be attributed to animal skin imperfections and non-uniformities, which are expected in natural animal skin. However, it is important to highlight that the fracture response is dominant. This scenario is a good approximation of a practical case, and therefore shows the relevance of the proposed MWI systemKesia C. Santos: Feasibility of Bone Fracture Detection using Microwave Imaging

It is worth recalling that the image inversion algorithm assumes uniform permittivity inside the bone. Also note that the actual permittivity of the animal bone may differ from the values used in the inversion algorithm. Despite these facts, the fracture detection and location in the case of a biological bone with skin were good, showing good robustness of the method to uncertainties that are expected in a real application. Experimental tests were performed also with bovine tibia bones (not shown), with equally positive results. The presented results show the relevance of the proposed MWI system.

VI. CONCLUSION

This study presented a method for detection and localization of transverse fractures in superficial bones using microwave imaging with a very simple setup that does not require immersion liquids and involves a single linear scanning antenna. The absence of the contact liquid poses new challenges, regarding skin artifact removal, which are tackled with proposed dedicated algorithms. The proposed algorithms also tackle non-uniformities of the bone and skin. The process was successfully tested by simulations and experiments on bone phantoms, and ex-vivo animal bone and skin.

The results showed that it is possible to detect and locate fractures as thin as 1 mm, even in the presence of non-uniformities of the bone boundary and its extra layers inside. The fracture detection and localization are not compromised by possible differences between the dielectric properties

assumed in the inversion algorithm and the actual ones of the phantom or the animal bone.

The proposed configuration is compatible with direct translation into a practical device for use in clinical applications. The results encourage the development of a portable setup for use with even more complete biological limb samples.

APPENDIX
See Table 4.

ACKNOWLEDGMENT

REFERENCES

[1] N. E. Jacob and M. Wyawahare, "Survey of bone fracture detection techniques," *Int. J. Comput. Appl.*, vol. 71, no. 17, pp. 31–34, Jun. 2013.

[2] G. D'Elia, G. Caracchini, L. Cavalli, and P. Innocentia, "Bone fragility and imaging techniques," *Clin. Cases Mineral Bone Metabolism*, vol. 6, pp. 234–246, Sep.–Dec. 2009.

[3] R. P. Ganesan, M. Palaniappan, S. Anbu, K. Kolundan, K. Kannan, and S. Karunanithi, "Elastic stable intramedullary nailing of femoral and tibial shaft fractures in children," *J. Evol. Med. Dental Sci.*, vol. 5, no. 4, pp. 5196–5201, Sep. 2016.

[4] P. Hadjizacharia *et al.*, "Lower extremity fractures in falls," *Eur. J. Trauma Emerg. Surgery*, vol. 40, no. 3, pp. 331–336, Jun. 2014.

[5] E. C. Fear, P. M. Meaney, and M. A. Stuchly, "Microwaves for breast cancer detection?" *IEEE Potentials*, vol. 22, no. 1, pp. 12–18, Feb./Mar. 2003.

[6] S. M. Sara, E. C. Fear, M. Okoniewski, and J. R. Matyas, "Exploring joint tissues with microwave imaging," *IEEE Trans. Microw. Theory Techn.*, vol. 58, no. 8, pp. 2307–2313, Aug. 2010.

[7] S. Mustafa, B. Mohammed, and A. Abbosh "Novel preprocessing techniques for accurate microwave imaging of human brain," *IEEE Antennas Wireless Propag. Lett.*, vol. 12, pp. 460–463, 2013.

[8] G. Ruvio, A. Cuccaro, R. Solimene, A. Brancaccio, B. Basile, and A. Ammann, "Microwave bone imaging: A preliminary scanning system for proof-of-concept," *Healthcare Technol. Lett.*, vol. 3, no. 3, pp. 218–221, Jun. 2016.

[9] B. Khalesi, B. Sohani, N. Ghavami, M. Ghavami, S. Dudley, and G. Tiberi, "A Phantom investigation to quantify huygens principle based microwave imaging for bone lesion detection," *Eletronics*, vol. 8, no. 12, p. 1505, Dec. 2019.

[10] B. Khalesi, B. Sohani, N. Ghavami, M. Ghavami, S. Dudley, and G. Tiberi, "Free space operating microwave imaging device for bone lesion detection: A phantom investigation," *IEEE Antennas Wireless Propag. Lett.*, vol. 19, no. 12, pp. 2393–2397, Dec. 2020.

[11] V. S. Ramalingam, M. Kanagasabai, and A. E. F. Sundarsingh, "A compact microwave device for fracture diagnosis of the human tibia," *IEEE Trans. Compon. Packag. Manuf. Technol.*, vol. 9, no. 4, pp. 661–668, Apr. 2019.

[12] K. C. Santos, C. A. Fernandes, and J. R. Costa, "A study on the sensitivity of microwave imaging for detecting small-width bone fractures," in *Proc. 15th Eur. Conf. Antennas Propag. (EUCAP)*, Apr. 2021, pp. 1–4.

[13] K. C. Santos, C. A. Fernandes, and J. R. Costa, "Experimental evaluation of thin bone fracture detection using microwave imaging," in *Proc. 16th Eur. Conf. Antennas Propag. (EUCAP)*, Apr. 2022, pp. 1–3.

[14] H. Gray, *Anatomy of the Human Body*, 20th ed. Philadelphia, PA, USA: Lea & Febiger, 1918.

[15] T. Karacolak, R. Cooper, E. S. Unlu, and E. Topsakal, "Dielectric properties of porcine skin tissue and in vivo testing of implantable antennas using pigs as model animals," *IEEE Antennas Wireless Propag. Lett.*, vol. 11, pp. 1686–1689, 2012.

[16] M. Vallejo, J. Recas, P. G. del Valle, and J. L. Ayala, "Accurate human tissue characterization for energy-efficient wireless on-body communications," *Sensors*, vol. 13, no. 6, pp. 7546–7569, Jun. 2013.

[17] N. Joachimowicz, C. Conessa, T. Henriksson, and B. Duchêne, "Breast phantoms for microwave imaging," *IEEE Antennas Wireless Propag. Lett.*, vol. 13, pp. 1333–1336, 2014.

[18] K. S. Sultan, B. Mohammed, P. C. Mills, and A. Abbosh, "Anthropomorphic durable realistic knee phantom for testing electromagnetic imaging systems," *IEEE J. Electromagn., RF, Microw. Med. Biol.*, vol. 5, no. 2, pp. 132–138, Jun. 2021.

[19] S. Gabriel, R. W. Lau, and C. Gabriel, "The dielectric properties of biological tissues: III. Parametric models for the dielectric spectrum," *Phys. Med. Biol.*, vol. 41, no. 11, pp. 2271–2293, 1996.

[20] C. Gabriel, "Dielectric properties of biological tissue: Variation with age," *Bioelectromagnetics*, vol. S7, pp. S12–S18, Jan. 2005.

[21] A. Peyman, C. Gabriel, E. H. Grant, G. Vermeeren, and L. Martens, "Variation of the dielectric properties of tissues with age: The effect on the values of SAR in children when exposed to walkie–talkie devices," *Phys. Med. Biol.*, vol. 54, pp. 227–242, Jan. 2009.

[22] M. Ibrani, L. Ahma, and A. E. Hamiti, "The age-dependence of microwave dielectric parameters of biological tissues," in *Microwave Materials Characterization*. Rijeka, Croatia: InTechOpen, 2012, pp. 139–158.

[23] N. Joachimowicz, B. Duchêne, C. Conessa, and O. Meyer, "Reference phantoms for microwave imaging," in *Proc. 11th Eur. Conf. Antennas Propag. (EUCAP)*, Paris, France, Mar. 2017, pp. 2719–2722.

[24] A. Kiourti, J. R. Costa, C. A. Fernandes, A. G. Santiago, and K. S. Nikita, "Miniature implantable antennas for biomedical telemetry: From simulation to realization," *IEEE Trans. Biomed. Eng.*, vol. 59, no. 11, pp. 3140–3147, Nov. 2012.

[25] A. La Gioia *et al.*, "Open-ended coaxial probe technique for dielectric measurement of biological tissues: Challenges and common practices," *Diagnostics*, vol. 8, pp. 1–38, Jun. 2018.

[26] D. Baudry, A. Louis, and B. Mazari, "Characterization of the open-ended coaxial probe used for near-field measurements on EMC applications," *Progr. Electromagn. Res.*, vol. 60, pp. 311–333, Jan. 2006.

[27] A. Kiourti, J. R. Costa, C. A. Fernandes, and K. S. Nikita, "A broadband implantable and a dual-band on-body repeater antenna: Design and transmission performance," *IEEE Trans. Antennas Propag.*, vol. 62, no. 6, pp. 2899–2908, Jun. 2014.

[28] J. M. Felício, "Antennas for biomedical applications: Wireless body area networks and medical imaging," Ph.D. dissertation, Dept. Electr. Comput. Eng., Tech. Univ. Lisbon, Lisbon, Portugal, 2018.

[29] E. J. Bond, X. Li, S. C. Hagness, and B. D. Van Veen, "Microwave imaging via space-time beamforming for early detection of breast cancer," *IEEE Trans. Antennas Propag.*, vol. 51, no. 8, pp. 1690–1705, Aug. 2003.

[30] J. M. Felício, J. M. Bioucas-Dias, J. R. Costa, and C. A. Fernandes, "Antenna design and near-field characterization for medical microwave imaging applications," *IEEE Trans. Antennas Propag.*, vol. 67, no. 7, pp. 4811–4824, Jul. 2019.

[31] M. A. Elahi, M. Glavin, E. Jones, and M. O'Halloran, "Artifact removal algorithms for microwave imaging of the breast," *Progr. Electromagn. Res.*, vol. 141, pp. 185–200, Jan. 2013.

[32] F. Abujarad, A. Jostingmeier, and A. S. Omar, "Clutter removal for landmine using different signal processing techniques," in *Proc. 10th Int. Conf. Grounds Penetrating Radar*, Jun. 2004, pp. 697–700.

[33] P. K. Verma, A. N. Gaikwad, D. Singh, and M. J. J. Nigam, "Analysis of clutter reduction techniques for through wall imaging in UWB range," *Progr. Electromagn. Res. B*, vol. 17, pp. 29–48, Jan. 2009.

[34] G. Ruvio, R. Solimene, A. Cuccaro, D. Gaetano, J. E. Browne, and M. J. Ammann, "Breast cancer detection using interferometric MUSIC experimental and numerical assessment," *Med. Phys.*, vol. 41, no. 10, pp. 1–11, Oct. 2014.

[35] J. M. Felício, J. M. Bioucas-Dias, J. R. Costa, and C. A. Fernandes, "Microwave breast imaging using a dry setup," *IEEE Trans. Comput. Imag.*, vol. 6, pp. 167–180, 2020, doi: 10.1109/TCI.2019.2931079.

[36] J. M. Lopez-Sanchez and J. Fortuny-Guasch, "3-D radar imaging using range migration techniques," *IEEE Trans. Antennas Propag.*, vol. 48, no. 5, pp. 728–737, May 2000.

[37] A. T. Mobashsher and A. M. Abbosh, "Performance of directional and omnidirectional antennas in wideband head imaging," *IEEE Antennas Wireless Propag. Lett.*, vol. 15, pp. 1618–1621, 2016.

[38] G. K. Pandey, H. S. Singh, P. K. Bhart, A. Pandey, and M. K. Meshram, "High gain vivaldi antenna for radar and microwave imaging applications," *Int. J. Signal Process. Syst.*, vol. 3, no. 1, pp. 35–39, Jun. 2015.

[39] F. R. de Souza, L. P. Alves, A. B. Villaverde, and E. Munin, "Assessment of age-related adaptive changes in relative transverse dimensions of the tibia and fibula: A preliminary study towards a different approach for age prediction in adults," *J. Foernsic Res.*, vol. 10, no. 2, Jul. 2019, Art. no. 1000444.

CARLOS A. FERNANDES (Senior Member, IEEE) received the Licenciado, M.Sc., and Ph.D. degrees in electrical and computer engineering from the Instituto Superior Técnico (IST), Technical University of Lisbon, Lisbon, Portugal, in 1980, 1985, and 1990, respectively.

In 1980, he joined IST, where he is currently a Full Professor with the Department of Electrical and Computer Engineering in the areas of microwaves, radio wave propagation and antennas. He is a Senior Researcher with the Instituto de Telecomunicacões, Lisbon, and a member of the Board of Directors. He has coauthored a book, two book chapters, more than 200 technical papers in peer reviewed international journals and conference proceedings and seven patents in the areas of antennas and radiowave propagation modeling. His current research interests include dielectric antennas for millimeter wave applications, antennas and propagation modeling for personal communication systems, RFID and UWB antennas, artificial dielectrics, and metamaterials.

Prof. Fernandes was the Guest Editor of the Special Issue on Antennas and Propagation at mm- and Sub mm-Waves, from the IEEE TRANSACTIONS ON ANTENNAS AND PROPAGATION, April 2013.

JORGE R. COSTA (Senior Member, IEEE) was born in Lisbon, Portugal, in 1974. He received the Licenciado and Ph.D. degrees in electrical and computer engineering from the Instituto Superior Técnico (IST), Technical University of Lisbon, Lisbon, in 1997 and 2002, respectively.

He is currently a Senior Researcher with the Instituto de Telecomunicações, Lisbon. He is also a Full Professor with the Departamento de Ciências e Tecnologias da Informação, Instituto Universitário de Lisboa (ISCTE-IUL). He is the coauthor of four patent applications and more than 200 contributions to peer-reviewed journals and international conference proceedings. More than 40 articles have appeared in IEEE journals. His current research interests include lenses, transmit-arrays, and biomedical antennas.

Dr. Costa was the Co-Chair of the Technical Program Committee of the European Conference on Antennas and Propagation (EuCAP 2015), Lisbon, and the General Vice-Chair of EuCAP 2017, Paris. He served as an Associate Editor for the IEEE TRANSACTIONS ON ANTENNAS AND PROPAGATION from 2010 and 2016. He is currently an Associate Editor of the IEEE OPEN JOURNAL OF ANTENNAS AND PROPAGATION. He was a Guest Editor of the IEEE TRANSACTIONS ON ANTENNAS AND PROPAGATION Special Issue on Antennas and Propagation at mm- and submm-Waves in 2013.

KESIA C. SANTOS (Student Member, IEEE) was born in João Pessoa, Brazil, 1981. She received the Technologist degree in telecommunications from the Federal Institute of Paraíba (IFPB), João Pessoa, in 2004, after completing a three-year education program, and the M.S.E.E. degree from the Federal University of Rio Grande do Norte, Natal, Brazil, in 2005. She is currently pursuing the Ph.D. degree with IST, Lisbon, Portugal.

Since 2010, she has been a Professor of Electronics and Antennas with IFPB. Her main interests include microwave imaging, biomedical solutions for low-income populations, design and development of antennas, encouragement actions to bring more girls to engineering.